On the use of a proton path probability map for proton computed tomography reconstruction[a)]

Dongxu Wang
Department of Medical Physics, University of Wisconsin School of Medicine and Public Health, Madison, Wisconsin 53792

T. Rockwell Mackie
Department of Medical Physics, University of Wisconsin School of Medicine and Public Health, Madison, Wisconsin 53792 and Department of Human Oncology, University of Wisconsin School of Medicine and Public Health, Madison, Wisconsin 53792

Wolfgang A. Tomé[b)]
Department of Medical Physics, University of Wisconsin School of Medicine and Public Health, Madison, Wisconsin 53792; Department of Human Oncology, University of Wisconsin School of Medicine and Public Health, Madison, Wisconsin 53792; Center for Medical Radiation Physics, University of Wollongong, Wollongong, NSW 2522, Australia

(Received 9 February 2010; revised 20 May 2010; accepted for publication 21 May 2010; published 20 July 2010)

Purpose: To describe a method to estimate the proton path in proton computed tomography (pCT) reconstruction, which is based on the probability of a proton passing through each point within an object to be imaged.
Methods: Based on multiple Coulomb scattering and a semianalytically derived model, the conditional probability of a proton passing through each point within the object given its incoming and exit condition is calculated in a Bayesian inference framework, employing data obtained from Monte Carlo simulation using GEANT4. The conditional probability at all of the points in the reconstruction plane forms a conditional probability map and can be used for pCT reconstruction.
Results: From the generated conditional probability map, a most-likely path (MLP) and a 90% probability envelope around the most-likely path can be extracted and used for pCT reconstruction. The reconstructed pCT image using the conditional probability map yields a smooth pCT image with minor artifacts. pCT reconstructions obtained using the extracted MLP and the 90% probability envelope compare well to reconstructions employing the method of cubic spline proton path estimation.
Conclusions: The conditional probability of a proton passing through each point in an object given its entrance and exit condition can be obtained using the proposed method. The extracted MLP and the 90% probability envelope match the proton path recorded in the GEANT4 simulation well. The generated probability map also provides a benchmark for comparing different path estimation methods. © *2010 American Association of Physicists in Medicine*. [DOI: 10.1118/1.3453767]

Key words: algebraic reconstruction, Bayesian inference, image reconstruction, most-likely path estimation, pCT reconstruction

I. INTRODUCTION

There has been a long-time interest in proton computed tomography (pCT). Imaging using high-energy proton projections is not only technologically feasible but may, in addition, have practical benefits. Unlike conventional x-ray CT, a pCT image will directly carry the information of proton stopping power or electron density, which should be more accurate than obtaining these quantities by calibrating and converting an x-ray CT image. Therefore, pCT is useful for treatment planning of proton therapy and may reduce the uncertainty in the delivery of proton radiation therapy. A proton beam of sufficient energy is required for pCT so that the object to be imaged is traversed by the proton beam and an image of the object can be reconstructed from measurements of the entrance energy, entrance position, entrance direction, residual exit energy, exit position, and exit direction of the protons. Since the dose is highest at their track end, i.e., in the Bragg peak, protons that traverse the imaged object will deposit only a relatively small dose along their path through the object. Hence, pCT could potentially also be a low dose imaging modality. In seminal work on pCT reconstruction, the proton energy fluence has been used for pCT reconstruction and proton scattering has been considered as a perturbation.[1–3] Recently, Li *et al.*[4] described a pCT reconstruction technique that employs the maximum-likelihood (ML) estimation of single proton paths to reconstruct pCT images. This ML proton path estimation technique allows one to take multiple Coulomb scattering (MCS) into account. This reconstruction scheme utilizes single proton information in a highly efficient manner and as a result, the reconstruction requires fewer protons per pixel than other proposed pCT reconstruction techniques. In the ML formalism

proposed by Schulte *et al.*,[5] the ML path of each proton is analytically calculated based on the available entrance and exit information of each proton. It has been further proposed that a probability envelope around the ML path could be employed for pCT reconstruction. In this work, we propose an alternative method for proton path estimation that can be employed to generate a proton path probability map, from which the most-likely path (MLP) and a probability envelope around the most-likely path can be extracted. Reconstruction of the pCT image is done using the full probability map, the extracted most-likely path, the extracted probability envelope, and a cubic spline path, respectively.

II. MATERIALS AND METHODS

II.A. Projection equation for algebraic reconstruction technique

Before we introduce our method for Bayesian inference-based proton path probability estimation, it is useful to review the algebraic reconstruction technique (ART) for pCT. The version of ART used in the present study is a simultaneous algebraic reconstruction technique (SART).[6] Penfold *et al.*[7] compared different versions of ART and variations thereof, and have found that they do not vary much in terms of the image quality achieved or their computational cost. Moreover, Tang *et al.*[8] also compared different iterative methods for the purpose of x-ray CT reconstruction and reached a similar conclusion.

Using the continuous slowing-down approximation, the differential energy loss at an arbitrary position (x,y) in the reconstruction plane is

$$-dE = S(x,y,E)dx, \tag{1}$$

where $S(x,y,E)$ is the stopping power in the material and dl is a differential path length.

Next we separate the energy and material factors from the stopping power by writing the stopping power as a product of mass stopping power and physical density of the material, and we furthermore multiply both sides of the relation by the mass stopping power of $E_0=200$ MeV at the arbitrary position (x,y) in the reconstruction plane

$$-\frac{S}{\rho}(x,y,E_0)dE = \frac{S}{\rho}(x,y,E_0)\cdot\frac{S}{\rho}(x,y,E)\cdot\rho(x,y)dl. \tag{2}$$

Dividing both sides by the mass stopping power at energy E for the material at the arbitrary point (x,y) in the reconstruction plane, we find

$$-\frac{\frac{S}{\rho}(x,y,E_0)}{\frac{S}{\rho}(x,y,E)}dE = S(x,y,E_0)dl. \tag{3}$$

Now observe that for the two materials considered in Fig. 1, which represent the minimal and maximal material densities present in the normal human body, the percentage error for the ratio of the mass stopping power at $E_0=200$ MeV to that of mass stopping power at energy E at an arbitrary reconstruction point (x,y) is less than 0.6% over the range of energy considered (data from NIST). Hence, the ratio of mass stopping powers on the left hand side depends only weakly on the material composition at the arbitrary point (x,y) in the reconstruction plane. We can therefore approximate the mass stopping power ratio for the material at the arbitrary point (x,y) in the reconstruction plane with the mass stopping power ratio of water.

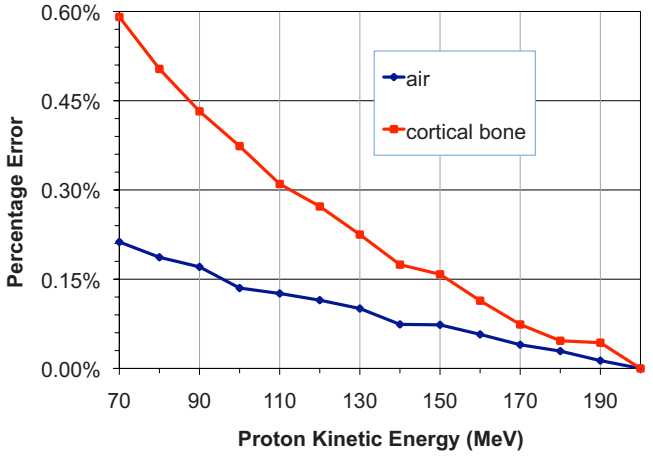

FIG. 1. Percentage error of the mass stopping power ratio of 200 MeV to that at energy E for the materials indicated compared to that of water.

$$\left[\frac{S}{\rho}(x,y)\right]_E^{E_0} \cong \left[\frac{S}{\rho}(\mathrm{H_2O})\right]_E^{E_0}, \tag{4}$$

where $\left[\frac{S}{\rho}(x,y)\right]_E^{E_0}$ is defined as $\left[\frac{S}{\rho}(x,y)\right]_E^{E_0} = \frac{S}{\rho}(x,y,E_0)/\frac{S}{\rho}(x,y,E)$.

Now using the approximation given in Eq. (4) for Eq. (3), we find

$$-\left[\frac{S}{\rho}(\mathrm{H_2O})\right]_E^{E_0}dE = S(x,y,E_0)dl. \tag{5}$$

The right hand side of Eq. (5) is the $E_0=200$ MeV stopping power at an arbitrary position of the proton path in the reconstruction plane. Integrating both sides of Eq. (5) along the proton path yields the following projection equation:

$$-\int_{E_{\mathrm{in}}}^{E_{\mathrm{out}}}\left[\frac{S}{\rho}(\mathrm{H_2O})\right]_E^{E_0}dE = \int_{\mathrm{path}} S(x,y,E_0)dl. \tag{6}$$

Using the projection equation given in Eq. (6), we can reconstruct the $E_0=200$ MeV stopping power value at any point in the reconstruction plane. Note that we can obtain this stopping power value at the reconstruction point without having to assume a specific material or its physical density at this reconstruction point. However, if the actual material and its physical density at each reconstruction point are known from some other imaging modality, then the reconstructed $E_0=200$ MeV stopping power values can be also used for quantitative calibration. Hence, Eq. (6) is the projection equation for a $E_0=200$ MeV stopping power image. For an image composed of N pixels, the equation for projection i can be written as follows:

$$p_i = -\int_{E_{\text{in}}}^{E_{\text{out}}} \left[\frac{S}{\rho}(\text{H}_2\text{O})\right]_E^{E_0} dE = \sum_{j=1}^{N} w_{ij} S_j(E_0). \tag{7}$$

Here p_i denotes the ray sum and w_{ij} denotes the path length of proton i through pixel j.

Using the form of the projection equation given in Eq. (7), an image with N pixels and M proton rays is given by the following set of equations:

$$\begin{aligned} &w_{11}S_1 + w_{12}S_2 + \cdots + w_{1N}S_N = p_1, \\ &w_{21}S_1 + w_{22}S_2 + \cdots + w_{2N}S_N = p_2 \\ &\vdots \\ &w_{M1}S_1 + w_{M2}S_2 + \cdots + w_{MN}S_N = p_M, \end{aligned} \tag{8}$$

where S_j is the E_0=200 MeV stopping power for pixel $j \in \{1, \cdots, N\}$. The goal of ART is to iteratively find the solution $\{S_j\}_{j\in\{1,\cdots,N\}}$ for the above equation set. For pCT reconstruction, the parameter set is determined from the proton path estimation. Even though we restricted ourselves to work with an initial proton energy E_0=200 MeV, the approximation we have made in Eq. (4) is also valid for proton energies higher than that and in fact improves with increasing proton energy. Therefore, our formalism can be employed over a range of initial proton energies.

II.B. Probability-based projection operation

In this section, we will explore an alternative expression of $\{w_{ij}\}_{i\in\{1,\cdots,M\},j\in\{1,\cdots,N\}}$ and its mathematical basis. The breaking up of a continuous image $f(x,y)$ into pixels can be modeled as expanding a continuous function $f(x,y)$ using a set of basis functions $b_j(x,y)$

$$f(x,y) = \sum_{j=1}^{N} g_j b_j(x,y), \tag{9}$$

where the basis functions $b_j(x,y)$ are given by

$$b_j(x,y) = \begin{cases} 1 & (x,y) \text{ inside pixel } j \\ 0 & \text{elsewhere} \end{cases} \tag{10}$$

and g_j is the image value on pixel j. In our case, it is the 200 MeV stopping power $g_j = S_j$.

The projection operation using Eq. (8) above can then be defined as follows:

$$p_i = R_i f(x,y) = \sum_{j=1}^{N} S_j R_i b_j(x,y) \equiv \sum_{j=1}^{N} w_{ij} S_j. \tag{11}$$

The projection operator R_i projects the basis function $b_j(x,y)$ onto the weight space yielding the weight w_{ij}, which is the path length of proton i inside each pixel j and needs to be calculated from the proton path estimation

$$R_i b_j(x,y) = w_{ij} = \begin{cases} \text{length of proton path in pixel } j, & \text{proton } i \text{ passes through pixel } j \\ 0, & \text{proton } i \text{ does not pass through pixel } j \end{cases}. \tag{12}$$

If one models the proton path as a probability map, i.e., one assumes that proton i has a certain probability of passing through pixel j, then one can reinterpret the projection operation on the basis functions $b_j(x,y)$ as follows:

$$R_i b_j(x,y) = w'_{ij}, \tag{13}$$

where w'_{ij} is now interpreted as the probability that proton i passes through pixel j, multiplied by a term in units of length to account for the correct dimension, i.e., one assumes that the proton is smeared across the image according to a to-be-determined probability distribution. We now embark on the derivation of such a probability distribution.

II.C. Bayesian inference-based proton path probability map

In what follows, we assume a uniform medium, unless stated otherwise. Referring to Fig. 2, we assume that a proton of energy E_0 is incident on the medium along the z-axis at the origin from the left. Upon entering the medium, it will undergo MCS (ignoring other effects since they are of second order), changing its direction and position along its path, ending up at a density and radiation length scaled depth z, $z = \rho / L_0 z_{\text{physical}}$, where L_0 denotes the radiation length of the medium. We denote the *probability* of this proton being deflected into the lateral position x and direction θ in the z-x plane by the distribution function $F(z,x,\theta)$. The form of $F(z,x,\theta)$ does not need to be specified for now as the general methodology is being introduced, though a modification of Fermi's form will be used as $F(z,x,\theta)$ later. Note that the lateral displacement x is also density and radiation length scaled.

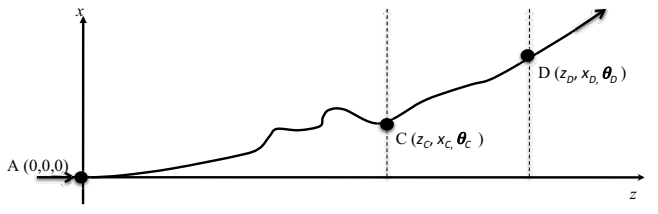

FIG. 2. Illustration of Bayesian inference-based proton path probability estimation. The proton enters at position A and exits at position D. The probability of the proton passing position C is to be estimated.

In Fig. 2, by construction, we have for the incoming condition $A\ (z_A, x_A, \theta_A)=(0,0,0)$, while we assume that we have the means of measuring the exit condition D_θ, which is given by (z_D, x_D, θ_D). The joint probability of a proton entering at incoming condition A passing through the intermediate condition $C_\theta(z_C, x_C, \theta_C)$ and then exiting the medium at exit condition D_θ can also be expressed in terms of the probability that the proton enters the medium at incoming condition A and exits the medium at exit condition D_θ and the conditional probability that the proton will pass through the intermediate condition C_θ given the exit condition D_θ

$$P(A \to C_\theta) \cdot P(C_\theta \to D_\theta) = P(A \to D_\theta) \cdot P(A \to C_\theta | D_\theta). \tag{14}$$

Here $P(X|Y)$ denotes the conditional probability, which specifies the probability that the proton has passed through condition X given that it is detected at exit condition Y. Hence, we can write the conditional probability $P(A \to C_\theta | D_\theta)$ as follows:

$$P(A \to C_\theta | D_\theta) = \frac{P(A \to C_\theta) \cdot P(C_\theta \to D_\theta)}{P(A \to D_\theta)}. \tag{15}$$

Note that the subscript θ indicates the conditions C and D are for a *specific direction* of the proton. For path estimation, however, we are interested in the probability $P(A \to C | D_\theta)$ that a proton moves through (z_C, x_C) *regardless of the direction at* C, given the specific exit condition D_θ

$$P(A \to C | D_\theta) = \frac{\int P(A \to C_\theta) \cdot P(C_\theta \to D_\theta) d\theta_C}{P(A \to D_\theta)}. \tag{16}$$

Given an incoming proton beam at A, $P(A \to C_\theta)$, $P(A \to D_\theta)$, and $P(C_\theta \to D_\theta)$ can all be expressed using the distribution function $F(z, x, \theta)$ as defined earlier, which will be given an exact form below. For proton i, the parameter w'_{ij} is just the conditional probability $P(\text{pixel } j | \text{exit})$ following the above calculation times a length term for having the correct dimension.

Note that we did not assume a specific form for the distribution function $F(z, x, \theta)$. The distribution function $F(z, x, \theta)$ could be chosen from MCS theory or could be determined by brute force through Monte Carlo simulation. In their review of cosmic ray theory using earlier work of Enrico Fermi, Rossi and Greisen[9] have derived the following form for the distribution function $F(z, x, \theta)$ based on MCS:

$$F(z,x,\theta) = \frac{\sqrt{3}}{2\pi}\frac{\omega^2}{z^2}\exp\left\{-\omega^2\left(\frac{\theta}{z} - \frac{3x\theta}{z^2} + \frac{3x^2}{z^3}\right)\right\}, \tag{17}$$

where z denotes the depth, x denotes the lateral defection at depth z projected into z-x plane, and θ is the direction relative to z-axis at depth z in z-x plane again. The term ω is related to energy of the incoming proton and is given by

$$\omega = \frac{2p\beta}{E_s}, \tag{18}$$

where the constant E_s has the dimension of energy and is given by $E_s = \mu_e\sqrt{4\pi/\alpha} = 21$ MeV; here μ_e denotes the rest mass of the electron and α denotes the fine-structure constant. Using the facts that $\gamma = (1-\beta^2)^{-(1/2)}$ and that the relativistic momentum can be written as $p = m_0 c\gamma\beta$, one easily finds that ω can be expressed as follows:

$$\omega = \frac{2\mu}{E_s c}\left(\gamma - \frac{1}{\gamma}\right), \tag{19}$$

where we denote by μ the rest mass of the proton in MeV. We will make use of this relationship below. As pointed out by Rossi and Greisen[9] for the case of MCS, the integration over θ can be extended over the entire real line [cf. Ref. 9, in particular, the discussion on page 266 following Eq. (1.59)]. We will, however, consider the effect of extending the integration over θ over the entire real line instead of restricting it to the forward scattering interval $[-\pi/2, \pi/2]$ on pCT reconstruction below. Integrating the distribution function from $(-\infty, \infty)$ over θ yields

$$H(z,x) = \int_{-\infty}^{+\infty} F(z,x,\theta)d\theta = \frac{\sqrt{3}}{2\sqrt{\pi}}\frac{\omega}{z^{3/2}}\exp\left(-\frac{3}{4}\frac{\omega^2 x^2}{z^3}\right). \tag{20}$$

This is the lateral position probability distribution at depth z, irrespective of angle. This probability distribution can be brought into standard Gaussian form, with zero mean and using the depth dependent variance $\sigma_z^2 = 2z^3/3\omega^2$. Various experimental studies have shown that a Gaussian distribution models the position and angular distribution of incoming heavy charged particles at a given depth in the medium well. In Fermi's derivation of $F(z, x, \theta)$, ω is assumed to be constant, which is certainly not true for the pCT application. Suppose our incoming protons have an energy of 200 MeV, after penetrating 20 cm water, the residual energy will be approximately 75 MeV. During this process, ω can vary by a factor of 3. In other words, ω is also highly dependent on the depth z. The Highland approximation[10] can be used to handle this problem; however, it requires integration along the z-direction of the proton beam. For fast evaluation of ω at a given depth z, the following approach has been implemented.

Since $H(z,x)$ is Gaussian, we assume $F(z,x,\theta)$ and $H(z,x)$ have the same general form as given in Eqs. (17) and (20), in which ω is replaced by a depth dependent term $u(z)$ to account for the energy loss along the proton's path. Then, the new forms of $F_u(z,x,\theta)$ and $H_u(z,x)$ are given by

$$F_u(z,x,\theta) = \frac{\sqrt{3}}{2\pi}\frac{u(z)^2}{z^2}\exp\left\{-u(z)^2\left(\frac{\theta^2}{z} - \frac{3x\theta}{z^2} + \frac{3x^2}{z^3}\right)\right\}, \tag{21}$$

$$H_u(z,x) = \frac{\sqrt{3}}{2\sqrt{\pi}}\frac{u(z)}{z^{3/2}}\exp\left(-\frac{3}{4}\frac{u(z)^2 x^2}{z^3}\right). \tag{22}$$

Because the variance of $H_u(z,x)$ can be determined from GEANT4 simulation at different depths in a homogenous me-

dium, $u(z)$ can be determined from simulation at different depths, eliminating the need to have an analytical expression for it. The $u(z)$ term can also be scaled by the incoming energy $u(z) \propto (\gamma - 1/\gamma)$ since Eq. (19) still holds over a certain energy range. Once $u(z)$ has been obtained, $F_u(z,x,\theta)$ can be determined, which can then be used to evaluate the path probability for protons of a given incoming energy

$$P(A \to C|D_\theta) = \frac{\int F_u(A \to C_\theta) \cdot F_u(C_\theta \to D_\theta) d\theta_C}{F_u(A \to D_\theta)}. \quad (23)$$

II.D. Simulation and reconstruction procedure

Using the GEANT4 Monte Carlo toolkit the depth dependent variance σ_z^2 was determined in water for protons having incoming energies of 175, 200, 225, and 250 MeV, respectively. Using the Monte Carlo derived values for the depth dependent variance, the function $u(z)$ for 200 MeV was then determined and used in the function $F_u(z,x,\theta)$ when calculating the conditional probability $P(\text{pixel } j|\text{exit})$.

To test our method, proton projections were simulated on a Shepp–Logan phantom.[11] 180 views of projections with 2° interval, each having 20 000 protons were used. For a 256 $\times$256 image, this corresponds to an average of 80 protons per pixel used for reconstruction. A virtual detector was used to record the position and momentum of each proton at the entrance and exit position in the reconstruction region. The entrance and exit information are then used to calculate the conditional probability that a given proton passes through each pixel of the image according to Eq. (16), i.e., the proton path is smeared over the image. Each conditional probability is normalized at the different depths, as expressed by a subset of pixels Γ_z, yielding

$$P_{ij} = \frac{P(\text{pixel } j|\text{exit})}{\sum_{j \in \Gamma_z} P(\text{pixel } j|\text{exit})}. \quad (24)$$

Because the reconstructed pixel values S_j are stopping powers, each normalized conditional probability P_{ij} is further scaled by the physical path length of proton, L_i, so that the projection Eq. (11) is met

$$p_i = \sum_{j=1}^{N} w'_{ij} S_j. \quad (25)$$

Although different path estimation methods give different path lengths L_i, for small angle scattering the path length is to first order well approximated by a straight line connecting the entrance and exit points. Thus,

$$w'_{ij} = \frac{P_{ij}}{\sum_{j=1}^{N} P_{ij}} L_i. \quad (26)$$

For reconstruction using only the extracted most-likely path or the probability envelope, the abovementioned normalization is done only on the pixels used.

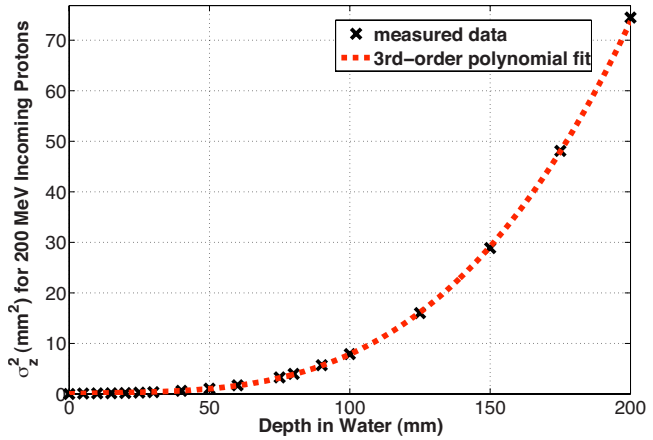

FIG. 3. Monte Carlo derived data for $\sigma_{10\ \text{cm}}(200\ \text{MeV})^2$ and the third-order polynomial fit of it.

At the beginning of the calculation, the whole reconstruction region is assumed to be water. Then iterative reconstruction for a 2 mm thick slice in the middle of Shepp–Logan phantom is done using SART.

III. RESULTS

III.A. The depth dependent variance σ_z in water for 200 MeV incoming protons as determined from simulation data

To facilitate reconstruction, the Monte Carlo derived data for σ_z^2 were fit using a third-order polynomial of z (in the original form derived by Rossi and Greisen, σ_z^2 is proportional to the third power of z), hence,

$$\sigma_z^2 = 0.000\,011\,6z^3 - 0.000\,582z^2 + 0.0207z. \quad (27)$$

Both σ_z and z are in units of mm in water. Monte Carlo simulated data for σ_z^2 together with its fit curve are shown in Fig. 3. Since we are assuming that the incoming protons form a differential pencil beam, there is no constant term in Eq. (27). By adding a constant term, it is possible to model a realistic incident proton distribution.

Once σ_z is determined $u(z)$ can be calculated as follows:

$$u(z) = \sqrt{\frac{2}{3}\frac{z^3}{\sigma_z^2}} \quad (28)$$

and can then be employed in the calculation of the conditional probability for each pixel using Eq. (23).

At this point, we would like to consider the effect the integration of the distribution function with respect to θ over the entire real line instead over the forward scattering interval $[-\pi/2, \pi/2]$ could have on pCT reconstruction. Integration of the proton distribution function over $[-\pi/2, \pi/2]$ yields

$$H(z,x) = \int_{-\pi/2}^{\pi/2} F(z,x,\theta) d\theta = \frac{\sqrt{3}}{4\sqrt{\pi}} \frac{\omega}{z^{3/2}} \exp\left(-\frac{4}{3}\frac{\omega^2 x^2}{z^3}\right) \times \left\{ \text{erf}\left[\frac{\omega(\pi z + 3x)}{2z^{3/2}}\right] + \text{erf}\left[\frac{\omega(\pi z - 3x)}{2z^{3/2}}\right] \right\}. \quad (29)$$

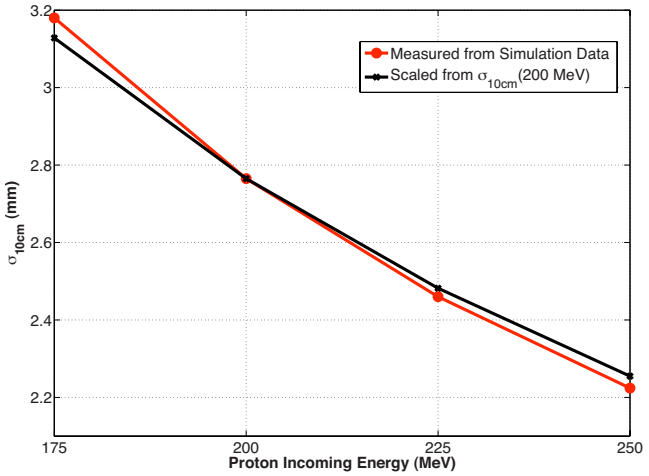

FIG. 4. $\sigma_{10\ \mathrm{cm}}(E)$ values measured from MC simulation and scaled from $\sigma_{10\ \mathrm{cm}}(200\ \mathrm{MeV})$.

For $x \ll z$, this simplifies to

$$H(z,x)\big|_{x\ll z} = \frac{\sqrt{3}}{2\sqrt{\pi}}\frac{\omega}{z^{3/2}}\exp\left(-\frac{4}{3}\frac{\omega^2 x^2}{z^3}\right)\mathrm{erf}\left(\frac{\omega\pi}{2\sqrt{z}}\right). \quad (30)$$

Note that the lateral distribution function given by Eq. (30) remains Gaussian with propagation in z. Since we have made no detailed assumptions regarding the functional form of $H(z,x)$ other than that it remains Gaussian, with propagation in z, the fit for the variance given in Eq. (27) is also applicable to this form of $H(z,x)$. Using the fit of σ_z^2 and its relationship with ω, the value of the error function $\mathrm{erf}(\pi\omega/2\sqrt{z})$ in Eq. (30) at different depths z can be evaluated, yielding a value that is equal to 1 for all $z > 0.1$ mm. Therefore, the error function does not affect the calculation or reconstruction when $x \ll z$, as is appropriate for MCS.

The value of the term $\mathrm{erf}[\omega(\pi z+3x)/2z^{3/2}]+\mathrm{erf}[\omega(\pi z-3x)/2z^{3/2}]$ in Eq. (29) without assuming $x \ll z$ can also be numerically evaluated. The value of this term is 2 for $z > 1.3\ x$, which includes the condition of MCS, and we are therefore justified to use the simple form for $H(z,x)$ given in Eq. (20).

III.B. Correction for the change in incoming energy by scaling $u(z)$

Using our derived scaling law for $u(z) \propto (\gamma - 1/\gamma)$, the values obtained for $u(z)$ from the 200 MeV data can be used to fit the Monte Carlo simulated data obtained for $u(z)$ for other energies as well. Figure 4 shows a comparison of the scaled and measured value of σ_z at a depth $z = 10$ cm. As seen from Fig. 4, the scaled ratio agrees with the measured one over a certain range of energy. Therefore, in practice, sampling a limited number of energies is sufficient for covering a large energy range.

III.C. Estimated proton paths

An example of a path probability map is shown in Fig. 5. Figure 5(a) shows the full probability map overlaid with the proton path obtained from the GEANT4 simulation (open squares with dashed line), extracted MLP (stars with dashed line), and CSP (open circles with dashed line); Fig. 5(b) shows 90% probability envelope (called MLP90) overlaid with the proton path obtained from the GEANT4 simulation (open squares with dashed line), the extracted MLP (stars with dashed line), and CSP (open circles with dashed line). The most-likely path is given by pixels that carry the highest conditional probability at each depth, i.e., the most-probable path. It can be shown that this most-probable path is equivalent to the most-likely path in the framework of maximum-likelihood estimation. Therefore, for consistency with the existing literature, we are using the terminology MLP in present study as well. The 90% probability envelope (MLP90) is given by all pixels that have a probability that is higher than 90% of the probability of the most-probable pixel at each depth.

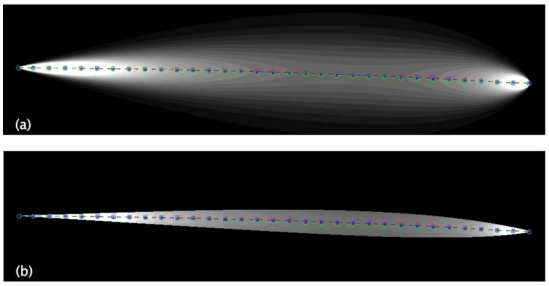

FIG. 5. A typical example of path estimation in 0.25 mm resolution. This path is 24 cm long in its original direction and the lateral deflection is 7.5 mm. (a) Full probability map overlaid with the real path (open squares with dashed line), extracted MLP (stars with dashed line), and CSP (open circles with dashed line); (b) 90% probability path envelope overlaid with the real path (open squares with dashed line), extracted MLP (stars with dashed line), and CSP (open circles with dashed line).

III.D. Image reconstructed using full probability map, extracted path, and extracted envelope

Images reconstructed using CSP, the full probability map, the MLP extracted from the probability map, and the MLP90 probability envelope are compared in Fig. 6. The projection data used are identical: 180 views, each view has 20 000 protons. Dose to the center of the phantom is 0.70 mGy as recorded by a dose tally during the GEANT4 simulation.

Using a full probability map [Fig. 6(b)] allows one to reconstruct a smoother image than any other path estimate for the proton path, though a pronounced dark ring artifact can be appreciated at the boundary between the bony shell and the brain tissue of the phantom. To a lesser extent, this artifact is present across all object boundaries in the phantom. We have traced this artifact back to the GEANT4 simulation and it appears that GEANT4 does not correctly model proton energy loss across object boundaries, which leads to estimates of stopping powers that are lower than their actual value across object boundaries, leading to the dark ring artifact present Fig. 6(b) at the boundary between the bony shell and the brain tissue when using the full probability map for pCT reconstruction. However, when one closely scrutinizes

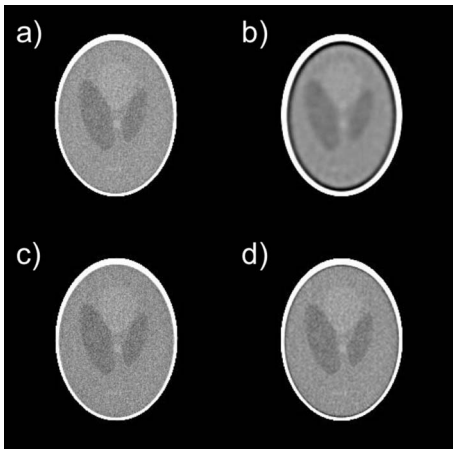

FIG. 6. Reconstruction of pCT using different proton path estimations. (a) One slice of a pCT image of the Shepp–Logan phantom reconstructed using CSP with bilinear interpolation; (b) the same slice reconstructed using the full probability map; (c) the same slice reconstructed using MLP extracted from the probability map; (d) the same slice reconstructed using the 90% probability envelope (MLP90).

the other pCT images that have been reconstructed using the other path estimation techniques, one finds that the dark ring artifact that is so pronounced in Fig. 6(b) is also present in these images, albeit masked by reconstruction noise.

Reconstruction using CSP with bilinear interpolation[6] shown in Fig. 6(a) and MLP shown in Fig. 6(c) are nearly equivalent in their performance, enabling visual detection of several of the elliptical shapes (ellipses B, C, D, and E, see Fig. 7) inside the phantom, whose density differences range from 2% to 4%. In Fig. 6(d), the 90% probability envelope (MLP90) is used for pCT image reconstruction with the result that the image is smoother than both the CSP reconstructed pCT image and the MLP reconstructed pCT image.

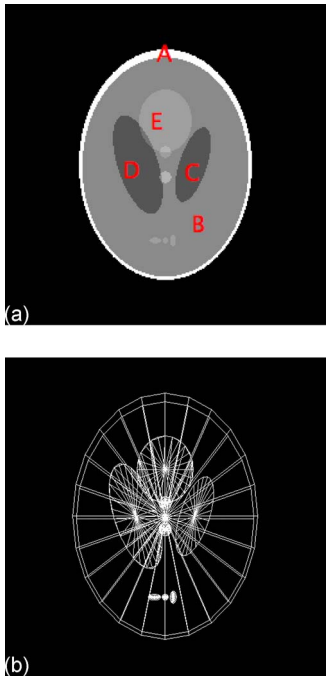

FIG. 7. (a) Densities in Shepp–Logan phantom [labeling follows the original label of Shepp and Logan (Ref. 11)]: Ellipse B: 1.02, C: 1.00, D: 1.00, and E: 1.03 g/cm^3. (b) The implemented Shepp–Logan phantom in GEANT4.

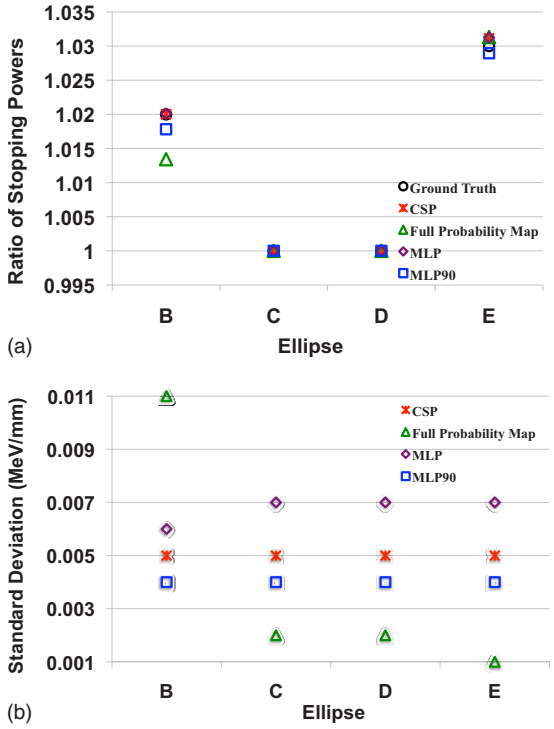

FIG. 8. (a) Ratio to stopping power in ellipse C and (b) standard deviations of stopping power values in selected regions of the image reconstructed using different path estimations. Refer to Fig. 7(a) for region labeling. For calculation of stopping power ratio, the average stopping power in ellipse C is considered to be 1. The ground truth values are the actual ratios used in simulation as defined by Shepp and Logan (Ref. 11).

III.E. Quantitative accuracy and noise characterization

For the purpose of treatment planning for proton radiation therapy, the quantitative systematic accuracy of the reconstructed pCT is important. The noise level is of lesser dosimetric importance, as noise in CT value does not degrade path length accuracy if the mean CT accuracy is maintained. However, noise level does degrade image clarity. Here we characterize the stopping power accuracy and noise by comparing the calibrated average and standard deviation of reconstructed 200 MeV stopping powers inside each of the elliptical shapes in the Shepp–Logan phantom. We assume the average stopping power in ellipse C, which consists of water, can always be accurately calibrated. Figure 7 shows the standard Shepp–Logan phantom we have used in our GEANT4 simulation with several major elliptical shapes labeled. The average and standard deviation from reconstructed images as well as the actual values are plotted in Figs. 8(a) and 8(b).

The CSP and MLP methods yield similar results for the accuracy of the reconstructed average stopping power inside

each of the elliptical shapes. However, the full probability map performs slightly worse, which is partly due to the dark ring artifact in ellipse B.

However, the full probability-map-based reconstruction method yields the least noisy image (except in ellipse B due to the dark ring artifact). The noise of the other three elliptical shapes are shown in Fig. 8(b) in the order of best to worst signal to noise ratio yields the following ordering of the path estimation methods MLP90, CSP, and MLP.

III.F. Computational cost

It is worth noting that because reconstruction involves more pixels in image space, the Bayesian inference-based proton path probability estimation is computationally more costly than the cubic spline path estimation method. For the reconstruction of a single pCT slice using the same projection data, the Bayesian inference-based proton path probability estimation scheme takes about one order of magnitude more time than the CSP estimation.

IV. CONCLUSION

In this work, detailed theoretical and computational schemes have been proposed and derived for the statistical estimation of proton path probability. The most-likely path or a path probability envelope can be extracted from the full probability map, and then used for pCT reconstruction. The full conditional probability map when used directly for pCT reconstruction yields a reconstructed image that is smoother than those obtained using the other path estimation methods. The most-likely path and the 90% probability envelope extracted from the full probability map perform similarly as the cubic spline path.

The CSP path consistently falls within the 90% probability envelope. Therefore, our path probability map provides a framework for explaining why cubic spline fitting may be an acceptable method for proton path estimation for pCT reconstruction.

ACKNOWLEDGMENTS

The authors would like to thank Reinhardt Schulte, Scott Penfold, Anatoly Rosenfeld, and Yair Censor for stimulating discussions regarding this as well as other subjects. In addition, the authors would like to thank the reviewers for their helpful and constructive comments, which have improved the presentation and quality of this paper. This work is supported in part by a grant from the National Cancer Institute Grant No. R01-109656.

[a]Conflicts of interest: The authors have no conflicts of interest in regards to the work reported on in this manuscript.
[b]Author to whom correspondence should be addressed. Electronic mail: tome@humonc.wisc.edu; Telephone: 608-263-8510; Fax: 608-263-9947.

[1]K. M. Hanson, J. N. Bradbury, T. M. Cannon, R. L. Hutson, D. B. Laubacher, R. Macek, M. A. Paciotti, and C. A. Taylor, "The application of protons to computed tomography," IEEE Trans. Nucl. Sci. **25**, 657–660 (1978).
[2]K. M. Hanson, J. N. Bradbury, R. A. Koeppe, R. J. Macek, D. R. Machen, R. Morgado, M. A. Paciotti, S. A. Sandford, and V. W. Steward, "Proton computed tomography of human specimens," Phys. Med. Biol. **27**, 25–36 (1982).
[3]P. Zygmanski, K. G. Gall, M. S. Z. Rabin, and S. J. Rosenthal, "The measurement of proton stopping power using proton-cone-beam computed tomography," Phys. Med. Biol. **45**, 511–528 (2000).
[4]T. F. Li, Z. R. Liang, J. V. Singanallur, T. J. Satogata, D. C. Williams, and R. W. Schulte, "Reconstruction for proton computed tomography by tracing proton trajectories: A Monte Carlo study," Med. Phys. **33**, 699–706 (2006).
[5]R. W. Schulte, S. N. Penfold, J. T. Tafas, and K. E. Schubert, "A maximum probability proton path formalism for application in proton computed tomography," Med. Phys. **35**, 4849–4856 (2008).
[6]A. H. Andersen and A. C. Kak, "Simultaneous algebraic reconstruction technique (SART): A superior implementation of the ART algorithm," Ultrason. Imaging **6**, 81–94 (1984).
[7]S. N. Penfold, R. W. Schulte, Y. Censor, V. Bashkirov, S. McAllister, K. E. Schubert, and A. B. Rosenfeld, "Block-iterative and string-averaging projection algorithms in proton computed tomography image reconstruction," in *Biomedical Mathematics: Promising Directions in Imaging, Therapy Planning and Inverse Problems*, edited by Y. Censor, M. Jiang, and G. Wang (Medical Physics Publishing, Madison, 2009).
[8]J. Tang, B. E. Nett, and G.-H. Chen, "Performance comparison between total variation (TV)-based compressed sensing and statistical iterative reconstruction algorithms," Phys. Med. Biol. **54**, 5781–5804 (2009).
[9]B. Rossi and K. Greisen, "Cosmic-ray theory," Rev. Mod. Phys. **13**, 240–309 (1941).
[10]V. L. Highland, "Some practical remarks on multiple scattering," Nucl. Instrum. Methods **129**, 497–499 (1975); "Erratum to some practical remarks on multiple scattering," **161**, 171 (1979).
[11]L. A. Shepp and B. F. Logan, "The Fourier reconstruction of a head phantom," IEEE Trans. Nucl. Sci. **NS-21**, 21–43 (1974).